nonlinear fracture mechanics theories[12] approximate, through tractions that resist crack opening, the net effects of various bridging mechanisms, such as bridging and frictional sliding between first-order lamellae and microcracking. Our micromechanical model predicts that the magnitudes of the bridging stresses, p, are proportional to the square root of the COD ($p = \beta\sqrt{\text{COD}}$), and are operative up to a critical opening COD_{cr}; here, β incorporates the effects of all possible energy-dissipating mechanisms. The additional energy associated with a fully developed bridging zone (whose tail has reached COD_{cr}) is given as:

$$J = \int_0^{(\text{COD}_{cr})} p(\text{COD})\text{d}(\text{COD}) = \frac{2}{3}\beta(\text{COD}_{cr})^{3/2}$$

We note that in this type of theory, which has been successful with other brittle matrix composites[12], the bridging law is the true material property.

Figure 4b shows load–displacement curves for a notched specimen (experiment A) and the 'calibration' simulation; a good fit to experiment is obtained using $\beta = 630\ \text{N m}^{-5/2}$ and $\text{COD}_{cr} = 5\ \mu\text{m}$ ($J = 0.15\ \text{N mm}^{-1}$). A comparison between the predictions of the now-calibrated bridging model and the experimental response of a notched beam of different dimensions (experiment B) is also shown in Fig. 4b. The model accurately predicts the behaviour of cracks propagating through the middle layer, and in turn, the effects of shell dimensions. The model can also predict the response of a multiply cracked unnotched shell sample, where final fracture results from the (stochastic) propagation through the middle layer of a single channel crack (simulation C). The load–deflection curve for this case suggests that the combination of multiple cracking and 'fibre' bridging increases the work of fracture by an additional order of magnitude.

A comparison of this last simulation with the mechanical response predicted for a crack growing self-similarly in a pure aragonite shell, or for a crack growing at 45° along an unbridged protein interface (see the inset of Fig. 4b) emphasizes the truly impressive fracture toughness of the shell of *Strombus gigas*. We consider that the microarchitecture of the *Strombus gigas* shell—that is, 'ceramic plywood'—could guide the design of lightweight structural composites. ☐

1. Wegst, U. G. K. & Ashby, M. F. Material selection charts for natural materials. Report No. CUED/C_EDC/TR55 (Cambridge Univ., 1997).
2. Taylor, J. D. & Layman, M. The mechanical properties of bivalve (mollusca) shell structures. *Palaeontology* **15**, 73–86 (1972).
3. Currey, J. D. & Taylor, J. D. The mechanical behaviour of some molluscan hard tissue. *J. Zool. Lond.* **173**, 395–406 (1974).
4. Currey, J. D. in *Mechanical Properties of Biological Materials* (eds Currey, J. D. & Vincent, J. F. V.) 75–97 (Cambridge Univ. Press, 1980).
5. Bøggild, O. B. The shell structure of the mollusks. *K. Danske Vidensk. Selsk. Skr.* **2**, 232–325 (1930).
6. Carter, J. G. in *Skeletal Growth of Aquatic Organisms* (eds Rhoads, D. C. & Lutz, R. A.) 69–113 (Plenum, New York, 1980).
7. Curry, J. D. & Kohn, A. J. Fracture in the crossed-lamellar structure of *Conus* shells. *J. Mater. Sci.* **11**, 1615–1623 (1976).
8. Jackson, A. P., Vincent, J. F. V. & Turner, R. M. The mechanical design of nacre. *Proc. R. Soc. Lond. B* **234**, 415–440 (1988).
9. Jackson, A. P., Vincent, J. F. V. & Turner, R. M. Comparison of nacre with other ceramic composites. *J. Mater. Sci.* **25**, 3173–3178 (1990).
10. Kuhn-Spearing, L. T., Kessler, H., Spearing, S. M., Ballarini, R. & Heuer, A. H. Fracture mechanisms of the *Strombus gigas* conch shell: Implication for the design of brittle laminates. *J. Mater. Sci.* **31**, 6583–6594 (1996).
11. Kessler, H., Ballarini, R., Mullen, R. L., Kuhn, L. T. & Heuer, A. H. A biomimetic example of brittle toughening: (I) steady state multiple cracking. *Comput. Mater. Sci.* **5**, 157–166 (1996).
12. Cox, B. & Marshall, D. B. Concepts for bridged cracks in fracture and fatigue. Overview No. 111. *Acta Metall. Mater.* **42**, 341–363 (1994).

Palaeotemperature reconstruction from noble gases in ground water taking into account equilibration with entrapped air

W. Aeschbach-Hertig*†, F. Peeters*, U. Beyerle* & R. Kipfer*‡

* Department of Water Resources and Drinking Water, Swiss Federal Institute of Environmental Science and Technology (EAWAG), CH-8600 Dübendorf, Switzerland
† Environmental Physics, ‡ Isotope Geology, Swiss Federal Institute of Technology (ETH), CH-8902 Zurich, Switzerland

Noble-gas concentrations in ground water have been used as a proxy for past air temperatures[1-7], but the accuracy of this approach has been limited by the existence of a temperature-independent component of the noble gases in ground water, termed 'excess air', whose origin and composition is poorly understood[7-9]. In particular, the evidence from noble gases in a Brazilian aquifer for a cooling of more than 5 °C in tropical America during the Last Glacial Maximum[4] has been called into question[9]. Here we propose a model for dissolved gases in ground water, which describes the formation of excess air by equilibration of ground water with entrapped air in quasi-saturated soils[10-12]. Our model predicts previously unexplained noble-gas data sets, including the concentration of atmospheric helium, and yields consistent results for the non-atmospheric helium isotopes that are used for dating ground water. Using this model of excess air, we re-evaluate the use of noble gases from ground water for reconstructing past temperatures. Our results corroborate the inferred cooling in Brazil during the Last Glacial Maximum[4], and indicate that even larger cooling took place at mid-latitudes.

Noble gases in ground water consist of three components: (1) dissolved air at solubility equilibrium, (2) certain isotopes from radioactive decay[13], and (3) "excess air"[8]. The temperature dependence of the first component has been used to infer recharge temperatures of ground water in order to reconstruct palaeotemperatures[1-7]. The second component is of importance for He (^{3}He from ^{3}H, ^{4}He from U/Th), and has been used extensively for groundwater dating[14-19]. Little is known about the origin and composition of the third component, although excess air may contain information about the environmental conditions pertaining during infiltration[7,20-22]. An understanding of the excess-air phenomenon is needed for the reliable calculation of noble-gas temperatures (NGTs) and groundwater ages.

Usually it is assumed that excess air is formed by total dissolution

Table 1 Statistical analysis of fits of excess-air models to noble-gas data sets

Data set	N	TD model χ^2	TD model P	PR model χ^2	PR model P	CE model χ^2	CE model P
Brazil	20	626.4	$< 10^{-14}$	71.8	9×10^{-8}	35.8	0.016
Oman	9	153.0	$< 10^{-14}$	55.2	1×10^{-8}	20.4	0.016
Maryland	20	246.8	$< 10^{-14}$	44.5	0.001	18.2	0.574
Belgium	28	303.6	$< 10^{-14}$	55.7	0.001	12.8	0.994
Belgium He*	28	358.6	$< 10^{-14}$	191.5	1×10^{-14}	34.2	0.990

N is the number of samples of each data set. χ^2 is the sum of the weighted squared deviations between modelled and measured noble-gas concentrations, summed over all samples of a data set[9,23]. The expected value of χ^2 is equal to the number of degrees of freedom, which is the number of fitted concentrations (4N, with He 5N) minus the number of free model parameters (2N (T, A_d) for the TD model, 3N (T, A_d, R or T, A_e, F) otherwise). P is the probability that χ^2 exceeds the observed value. Models with P < 0.01 are rejected.
* Belgian data set with the calculated He$_{atm}$ (Methods, Fig. 1) as additional constraint.
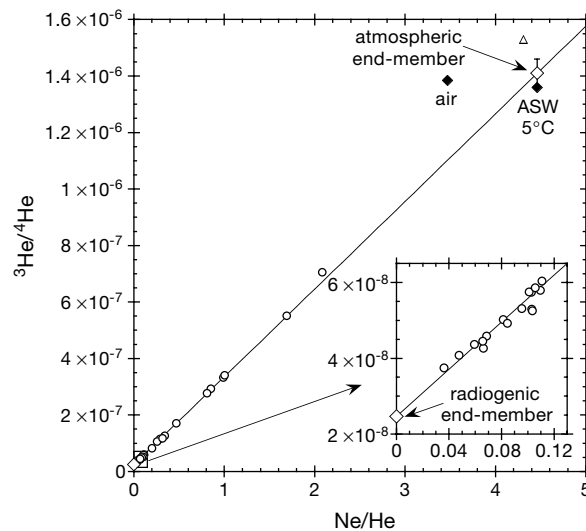
Figure 1 He isotope ratio versus Ne/He elemental ratio of samples from Belgium. The data define a mixing line between a radiogenic and an atmospheric end-member. The linear regression was calculated by a least-squares fit weighted with both x and y errors (errors are similar to the size of the symbols). One sample (triangle) from a shallow well in the recharge area appears to be affected by ^{3}He from the decay of bomb tritium, and was thus excluded from the fit. The point for air-saturated water (ASW) is shown for the representative temperature of 5 °C.

of small air bubbles trapped in soil pores[2,3,5,8]. In this total dissolution (TD) model, the concentrations of dissolved atmospheric gases are[23]:

$$C_i(T, S, P, A_d) = C_i^*(T, S, P) + A_d z_i \qquad (1)$$

where $C_i^*(T, S, P)$ are the moist-air solubility equilibrium concentrations as functions of temperature, salinity, and atmospheric pressure, A_d is the concentration of totally dissolved dry air, and z_i are the volume fractions of the individual gases in dry air. However, because the TD model does not yield consistent NGTs for the noble-gas record from Brazil, a model of excess-air fractionation by partial diffusive re-equilibration (PR model) was introduced[4], which may be written as[23]:

$$C_i(T, S, P, A_d, R) = C_i^*(T, S, P) + A_d z_i e^{-R\frac{D_i}{D_{Ne}}} \qquad (2)$$

where R is a parameter describing the degree of re-equilibration and D_i are the molecular diffusion coefficients. Yet, even the PR model does not provide an adequate description of the Brazilian noble-gas data[9].

Here we propose a new model explaining excess air as the result of equilibration of ground water with persistent entrapped air. The occurrence of air entrapment during groundwater infiltration is well known[10–12], but has never been quantitatively linked to the phenomenon of excess air. The basic assumption of our model is that solubility equilibrium is attained in a closed system of initially air-saturated water and a finite volume of entrapped air under a constant hydrostatic pressure. The equations of this closed-system equilibration (CE) model are:

$$C_i(T, S, P, A_e, F) = C_i^*(T, S, P) + \frac{(1-F)A_e z_i}{1 + FA_e z_i / C_i^*} \qquad (3)$$

where A_e is the initial amount of entrapped air per unit mass of water and F is the fractionation parameter (Methods). Note that A_e (entrapped air) is the same as A_d (dissolved air) only in the case of total dissolution. F is the ratio of two parameters with a clear physical meaning: v, the ratio of the entrapped gas volumes in the final and initial state, and q, the ratio of the dry gas pressure in the trapped gas to that in the free atmosphere. The values of v and q can be calculated from $F = v/q$ and A_e, using the condition that the sum of all partial pressures in the trapped volume equals the total pressure. Equation (3) describes all possible cases between no excess air ($F = v = q = 1$), pure excess air ($F = 0$, $v = 0$ or q infinite), and a pure pressure effect, that is, equilibration with the atmosphere at increased pressure ($v = 1$, $q > 1$, $F = 1/q < 1$, A_e infinite). Thus, it is a very general description of the concentrations of dissolved gases in ground water.

Equations (1) to (3) describe the concentrations of Ne, Ar, Kr and Xe (He is usually affected by non-atmospheric sources) with up to five parameters. In practice, S and P are usually known ($S \approx 0$ for meteoric water, and P can be calculated from the altitude of the recharge area). The remaining unknown parameters have traditionally been determined by iteration[3,4,7]. Recently, weighted least-squares techniques to invert the model equations have been developed, enabling quantitative assessment of the ability of different conceptual models to explain the observations[9,23].

We checked the practical applicability of the models by fitting them to two noble-gas data sets from tropical regions, northeastern Brazil[4] and Oman[6], and two from temperate regions, Maryland (USA)[24] and Belgium. The goodness of fit was quantified by applying the χ^2 test to the ensemble of the samples of each data set[9,23] (Table 1). Although the PR model performs far better than the TD model, it does not describe the observed noble-gas concentrations within their experimental uncertainty. In all cases, only the CE model yields an acceptable description of the data. The physical plausibility of the CE model can be checked by comparing the results obtained for its physically interpretable parameters with empirical findings on entrapped air and excess air (Table 2). The

Table 2 Values of excess-air parameters obtained from fits of the CE model

Data set	A_e	v	q	F
Brazil	0.017 ± 0.005	0.53 ± 0.19	1.56 ± 0.29	0.37 ± 0.17
Oman	0.025 ± 0.020	0.78 ± 0.12	1.31 ± 0.19	0.61 ± 0.14
Maryland	0.049 ± 0.059	0.88 ± 0.07	1.16 ± 0.04	0.76 ± 0.06
Belgium	0.083 ± 0.074	0.91 ± 0.08	1.16 ± 0.08	0.79 ± 0.09
Expected*	0.02–0.18	~0.9	~1.2	~0.75

A_e is given in cm^3 STP g^{-1}; the other parameters are dimensionless. Mean values and standard deviations of the results from the individual samples are given.
* Expected values were derived from empirical field data as follows. A_e: entrapped air was found to occupy between 2% and 15% of the pore space (corresponding to 2–18% of water volume) during groundwater infiltration[11]. v: Typical concentrations of dissolved excess air are of the order of 0.001 to 0.01 cm^3 STP g^{-1} (10–100% ΔNe)[3–5,7,23], indicating dissolution of only about 10% of A_e, and hence corresponding to v-values of about 0.9. q: air entrapment occurs in the uppermost metres of the aquifer, where the water table fluctuates[11,12]. q increases above 1 by about 0.1 per metre of hydrostatic overload. F: from $F = v/q$.

 1041

Table 3 Model dependence of non-atmospheric He components and corresponding ages

	Maryland: 4 young samples		Switzerland: 5 fractionated samples		
Model	$^4He_{rad}$ (10^{-9} cm^3 STP g^{-1})	^{4}He age (yr)	$^4He_{rad}$ (10^{-9} cm^3 STP g^{-1})	$^3He_{tri}$ (10^{-15} cm^3 STP g^{-1})	^{3}H–^{3}He age (yr)
TD model	-1.0 ± 0.8	-630 ± 490	-0.5 ± 0.8	-0.1 ± 1.4	0.0 ± 0.4
PR model	7.8 ± 2.3	$4,700 \pm 1,400$	5.9 ± 1.2	9.4 ± 2.0	2.4 ± 0.5
CE model	0.3 ± 0.5	210 ± 290	0.6 ± 0.9	1.4 ± 1.4	0.4 ± 0.4
Expected*	< 0.08	< 50	0.8 ± 0.4	3.1 ± 1.3	0.8 ± 0.3

Mean values and standard deviations of the results from the individual samples are given.
* Expected values were derived as follows. Maryland: the 4 samples discussed here are from shallow wells in the recharge area and must be less than 50 yr old according to ^{3}H and ^{3}He data. Conversion between $^4He_{rad}$ and ages is done using the *in situ* production rate of 1.6×10^{-12} cm^3 STP g^{-1} yr^{-1}, derived from U and Th analyses on sediment samples and supported by ^{14}C ages[24]. Switzerland: the 5 samples discussed here, all from one particular sampling date, are the only ones with fractionated excess air out of a data set of 48 samples[17,23]. Expected results were estimated based on 10 samples from the same boreholes but other sampling dates.

data sets from Maryland and Belgium yield values within the expected range. The two tropical records yield higher values of q and lower values of A_e and v. This finding may reflect actual differences in the infiltration regime, for example, larger water-table fluctuations (higher q) in the tropical aquifers.

The conclusion that only the CE model provides a realistic description of the data is further supported by an analysis of the usually neglected He data. Because of its low solubility and high diffusivity, He reacts most sensitively to excess air and to diffusive fractionation. However, most palaeogroundwaters contain large excesses of non-atmospheric, usually radiogenic, He. Atmospheric (He_{atm}) and radiogenic (He_{rad}) He components may be separated based on their very different ^{3}He/^{4}He ratios[25]. Our data from Belgium define a two-component mixing line between a radiogenic and an atmospheric end-member (Fig. 1). Based on the position along this line, each sample was split into its components (Methods).
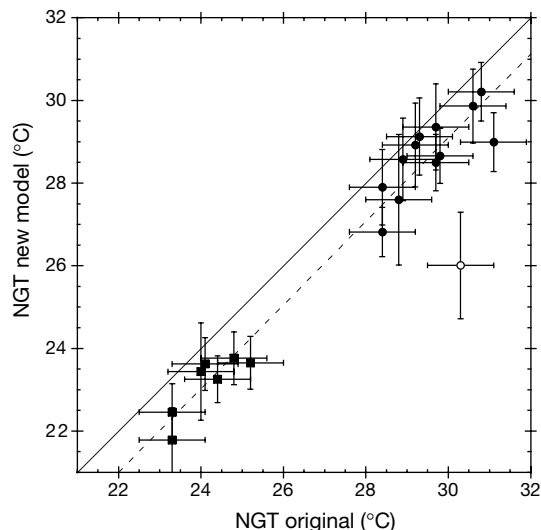

Figure 2 Comparison of new and original noble gas temperatures (NGTs) from Brazil. In the original publication[4], NGTs were calculated using an iterative technique to correct for fractionated excess air according to the PR model. We re-evaluated NGTs by inversion of the new CE model for fractionated excess air. Symbols reflect the clusters of samples identified in the original work: filled circles correspond to high temperatures and low ^{14}C-ages, filled squares to lower temperatures and higher ages, and the open circle refers to a special sample (no. 17) which for several reasons was omitted in calculating the glacial–interglacial temperature difference[4]. The regression line (dashed) through the data (excluding sample 17) is practically parallel to the 1:1 line (solid), and indicates that the new NGTs are on average 1 °C lower than the original values. The mean new NGT of the warm cluster is 28.7 ± 0.3 °C (compared to 29.6 °C in the original evaluation) in good agreement with the mean local ground temperature of 29.1 °C. The cool cluster yields a mean NGT of 23.1 ± 0.3 °C (original value 24.2 °C). We note that temperature difference between warm and cold clusters remains practically unchanged (5.6 ± 0.4 °C).

The calculated He_{atm} was then used as a fifth, excess air sensitive, constraint in the inversion of equations (1) to (3). With this additional constraint, the CE model still provides a good fit, whereas the PR model becomes clearly unacceptable (Table 1).

The predictions of the PR and CE models for He_{atm} differ strongly due to high diffusive He loss in the PR model. This fact has consequences for groundwater dating based on the accumulation of radiogenic $^4He_{rad}$ and tritiogenic $^3He_{tri}$. These He components are best determined by measuring all noble gases, and using the parameters derived from the inverse modelling of the heavier noble gases to calculate He_{atm}. We used this approach to calculate $^4He_{rad}$ in samples from the recharge area of the coastal aquifer in Maryland[24] as well as $^4He_{rad}$ and $^3He_{tri}$ in samples from a shallow alluvial aquifer in Switzerland[17,23]. In both examples, we can estimate the expected results (Table 3). The TD model implies obviously inconsistent negative values of the non-atmospheric He components and corresponding ages. The PR model yields unrealistically high ages. Only the results obtained with the CE model are in accordance with expectations.

For dating with He isotopes, usually only Ne is measured to calculate He_{atm}, based on the assumption that excess air has the atmospheric He/Ne ratio of 0.288 (TD model)[14–17]. As in our examples, this assumption sometimes leads to negative ages[16,17]. This inconsistency can be resolved by assuming fractionated excess air with a lower He/Ne ratio. In contrast to the PR model, the CE model predicts a lower limit of the excess air He/Ne ratio, given by the value for equilibrated water (0.22 to 0.25, depending on temperature). This value can be used to define an upper boundary for non-atmospheric He components and related ages. Our results highlight the advantage of combining analyses of He isotopes and atmospheric noble gases. He data may be useful to identify excess air fractionation and hence to obtain more reliable NGTs. Conversely, atmospheric noble-gas data provide a firm basis for the calculation of the non-atmospheric ^{4}He and ^{3}He components needed for dating.

The most important implications of our excess air model concern the reliability of noble-gas palaeoclimate records, particularly with regard to the controversial issue of tropical temperatures during the Last Glacial Maximum. The discrepancy between weak glacial cooling (≤ 2 °C) indicated by most oceanic palaeoclimate proxies[26,27], and a strong temperature change (~ 5 °C) indicated by continental records[4,28,29], is still not entirely explained.

The reliability of the important evidence for a large continental cooling provided by the Brazilian noble-gas study depends on an appropriate understanding of excess air. The original interpretation was based on the PR model[4], which is inconsistent with the data[9] (Table 1). Applying the CE model and the inverse fitting procedure[23], we obtain consistent new NGTs that are systematically lower than the original values by about 1 °C (Fig. 2). The data form two clusters, one corresponding to high temperatures and low ^{14}C ages, the other to lower temperatures and higher ages. The temperature difference between the clusters is 5.6 ± 0.4 °C, indistin-

guishable from the original result of $5.4 \pm 0.6\,°C$. Our internally consistent and mathematically rigorous analysis of the data reinforces the conclusion of a $\sim 5\,°C$ glacial–interglacial temperature difference in tropical Brazil. The hypothesis of a large tropical cooling is further supported by recent noble-gas records indicating a glacial cooling of $6.5\,°C$ in Oman[6] and $5.3\,°C$ in Namibia[22]. Whereas the Oman data could only be interpreted with the new CE model, the results from Namibia were based on the PR model and may need to be re-evaluated.

The CE model is crucial for a consistent interpretation not only of the tropical noble-gas records, but also those from Maryland and Belgium (Table 1). NGTs calculated with the CE model suggest an even larger ($7–9\,°C$) glacial cooling for these mid-latitude records. The original interpretation of other noble-gas data sets from temperate regions was based on the TD model and has also been questioned[9]. We expect that a re-evaluation of these data will primarily affect the individual NGTs rather than the reconstructed glacial–interglacial temperature difference, as exemplified by the Brazilian record. The inverse technique of calculating NGTs[9,23] and the view of excess air described here provide a mathematically and physically sound theoretical foundation for the noble-gas palaeothermometer. The resulting reliable NGTs may be used to calibrate the ^{18}O palaeothermometer by simultaneous analysis of noble gases and ^{18}O in aquifers[5].

Finally, our model provides a link between investigations of dissolved gases in ground water and the study of air entrapment in quasi-saturated soils. We are currently investigating relationships between entrapped air, excess air, fractionation, and infiltration conditions in laboratory and field studies. Eventually, excess air may provide information just as important as that derived from the other noble-gas components in ground water. □

Methods

Model derivation

According to Henry's law, at solubility equilibrium the gas concentrations C_i in solution are proportional to the partial pressures p_i in the gas phase:

$$p_i = H_i(T,S)C_i \tag{4}$$

where $H_i(T,S)$ is the Henry coefficient, depending on temperature T and salinity S.

We describe a closed system consisting of a water volume V_w and an initial trapped air volume V_g^0 under a constant total pressure $P_g = P + P_h$, where P is the atmospheric and P_h the hydrostatic pressure. In the initial state, the dissolved gas concentrations are in atmospheric solubility equilibrium[23]:

$$C_i^*(T,S,P) = \frac{p_i^{atm}}{H_i(T,S)} = \frac{(P - e(T))z_i}{H_i(T,S)} \tag{5}$$

where $e(T)$ is the saturation water vapour pressure and z_i are the volume fractions in dry air. The volume at STP of dry entrapped air per unit mass of water is:

$$A_e = \frac{V_g^0}{\rho(T,S)V_w} \frac{(P_g - e(T))}{P_0} \tag{6}$$

where $\rho(T,S)$ is the water density, and P_0 is the standard pressure (1 atm).

In the final state, a gas volume V_g remains and equilibrium is achieved, that is, all gases partition between V_g and V_w according to Henry's law, equation (4). In a closed system, the total gas amounts must be conserved, that is, the sum of the number of moles of each gas in the water and the gas phase is equal in the initial and the final state.

$$n_{i,w}^0 + n_{i,g}^0 = n_{i,w} + n_{i,g} \tag{7}$$

Inserting equations (4) to (6) into (7) and using the ideal-gas law leads to equations that describe the concentrations of dissolved gases in the water in the final state:

$$C_i = (C_i^* + A_e z_i)\left(1 + \frac{V_g}{V_w}\frac{(P-e)z_i}{\rho P_0 C_i^*}\right)^{-1} \tag{8}$$

where $C_i^* = C_i^*(T,S,P)$ are the moist air solubility equilibrium concentrations as in equation (5). By defining $v = V_g/V_g^0$, $q = (P_g - e)/(P - e)$, and $F = v/q$, we finally arrive at the model equations (3).

Separation of He components

Because the radiogenic He component (He$_{rad}$) is highly variable and can be overwhel-

---

mingly large, the measured concentrations of ^4He or total He (He$_{meas}$) provide no information on the atmospheric He component (He$_{atm}$) to be used to invert the model equations (1) to (3). However, because the typical radiogenic $^3He/^4He$ ratio ($R_{rad} \approx 2 \times 10^{-8}$) is two orders of magnitude smaller than that of the atmospheric sub-components (air: $R_a = 1.384 \times 10^{-6}$, air-saturated water: $R_{asw} \approx 0.983\,R_a$; ref. 30), the radiogenic component is much less dominant for ^3He. If He$_{meas}$ in a given aquifer results from a simple two-component mixture of He$_{atm}$ and He$_{rad}$, both with uniform isotopic compositions R_{atm} and R_{rad}, measuring both He isotopes yields information on He$_{atm}$. To extract this information, we have to use the ensemble of the data set.

A plot of the measured $^3He/^4He$ isotope ratio versus the Ne/He elemental ratio can serve both as a check of the two-component mixing hypothesis as well as to define the isotopic composition of the end-members. The excellent linear correlation in our example from Belgium (Fig. 1) confirms that each sample is essentially a mixture of two end-members. The intercept of the regression line (calculated by a least-squares fit weighted with both x and y errors) at Ne/He $= 0$ defines $R_{rad} = (2.47 \pm 0.20) \times 10^{-8}$, typical for radiogenic He. The atmospheric end-member must lie on the regression line in the vicinity of the point for air-saturated water (ASW). Addition of ^3He from the decay of natural (pre-bomb) tritium shifts the end-member slightly upwards. We take the $^3He/^4He$ ratio defined by the regression line at the Ne/He value of the ASW point as the best estimate for R_{atm}, with an uncertainty large enough to include R_{asw}, yielding $R_{atm} = (1.41 \pm 0.05) \times 10^{-6}$.

The measured He isotope ratios (R_{meas}) reflect the mixing ratios of the two end-members. Using R_{atm} and R_{rad} defined from the entire data set, the contribution of He$_{atm}$ to each individual sample can be calculated:

$$He_{atm} = He_{meas}\frac{(R_{meas} - R_{rad})}{(R_{atm} - R_{rad})} \tag{9}$$

In the Belgian data set, the uncertainty of the calculated He$_{atm}$ ranges from 4% (due to the uncertainty in R_{atm}) up to 15% for the samples with the highest He$_{rad}$. Even this limited precision is however sufficient to distinguish between the PR and CE models, because their predictions for He$_{atm}$ are very different (Table 1).

1. Mazor, E. Paleotemperatures and other hydrological parameters deduced from gases dissolved in groundwaters, Jordan Rift Valley, Israel. *Geochem. Cosmochim. Acta* **36**, 1321–1336 (1972).
2. Andrews, J. N. & Lee, D. J. Inert gases in groundwater from the Bunter Sandstone of England as indicators of age and palaeoclimatic trends. *J. Hydrol.* **41**, 233–252 (1979).
3. Stute, M. & Schlosser, P. in *Climate Change in Continental Isotopic Records* (eds Swart, P. K., Lohmann, K. C., McKenzie, J. & Savin, S.) 89–100 (American Geophysical Union, Washington DC, 1993).
4. Stute, M. *et al.* Cooling of tropical Brazil (5 °C) during the Last Glacial Maximum. *Science* **269**, 379–383 (1995).
5. Beyerle, U. *et al.* Climate and groundwater recharge during the last glaciation in an ice-covered region. *Science* **282**, 731–734 (1998).
6. Weyhenmeyer, C. E. *et al.* Cool glacial temperatures and changes in moisture source recorded in Oman groundwaters. *Science* **287**, 842–845 (2000).
7. Stute, M. & Schlosser, P. in *Environmental Tracers in Subsurface Hydrology* (eds Cook, P. & Herczeg, A. L.) 349–377 (Kluwer Academic, Boston, 2000).
8. Heaton, T. H. E. & Vogel, J. C. "Excess air" in groundwater. *J. Hydrol.* **50**, 201–216 (1981).
9. Ballentine, C. J. & Hall, C. M. An inverse technique for calculating paleotemperatures and other variables using noble gas concentrations in groundwater. *Geochim. Cosmochim. Acta* **63**, 2315–2336 (1999).
10. Christiansen, J. E. Effect of entrapped air upon the permeability of soils. *Soil Sci.* **58**, 355–365 (1944).
11. Fayer, M. J. & Hillel, D. Air encapsulation: 1. Measurement in a field soil. *Soil Sci. Soc. Am. J.* **50**, 568–572 (1986).
12. Faybishenko, B. A. Hydraulic behavior of quasi-saturated soils in the presence of entrapped air: Laboratory experiments. *Wat. Resour. Res.* **31**, 2421–2435 (1995).
13. Lehmann, B. E. & Purtschert, R. Radioisotope dynamics – the origin and fate of nuclides in groundwater. *Appl. Geochem.* **12**, 727–738 (1997).
14. Schlosser, P., Stute, M., Sonntag, C. & Münnich, K. O. Tritiogenic ^3He in shallow groundwater. *Earth Planet. Sci. Lett.* **94**, 245–256 (1989).
15. Aeschbach-Hertig, W. *et al.* A $^3H/^3He$ study of ground water flow in a fractured bedrock aquifer. *Ground Wat.* **36**, 661–670 (1998).
16. Dunkle Shapiro, S., Rowe, G., Schlosser, P., Ludin, A. & Stute, M. Tritium-helium 3 dating under complex conditions in hydraulically stressed areas of a buried-valley aquifer. *Wat. Resour. Res.* **34**, 1165–1180 (1998).
17. Beyerle, U. *et al.* Infiltration of river water to a shallow aquifer investigated with $^3H/^3He$, noble gases and CFCs. *J. Hydrol.* **220**, 169–185 (1999).
18. Solomon, D. K., Hunt, A. & Poreda, R. J. Source of radiogenic helium 4 in shallow aquifers: Implications for dating young groundwater. *Wat. Resour. Res.* **32**, 1805–1813 (1996).
19. Osenbrück, K., Lippmann, J. & Sonntag, C. Dating very old pore waters in impermeable rocks by noble gas isotopes. *Geochim. Cosmochim. Acta* **62**, 3041–3045 (1998).
20. Heaton, T. H. E., Talma, A. S. & Vogel, J. C. Origin and history of nitrate in confined groundwater in the western Kalahari. *J. Hydrol.* **62**, 243–262 (1983).
21. Wilson, G. B. & McNeill, G. W. Noble gas recharge temperatures and the excess air component. *Appl. Geochem.* **12**, 747–762 (1997).
22. Stute, M. & Talma, A. S. in *Isotope Techniques in the Study of Environmental Change* 307–318 (IAEA, Vienna, Austria, 1998).
23. Aeschbach-Hertig, W., Peeters, F., Beyerle, U. & Kipfer, R. Interpretation of dissolved atmospheric noble gases in natural waters. *Wat. Resour. Res.* **35**, 2779–2792 (1999).
24. Aeschbach-Hertig, W., Stute, M., Schlosser, P., Clark, J. & Reuter, R. Large (9°C) glacial-interglacial temperature difference derived from an aquifer in Maryland (abstr.). *Eos* **77**, (Suppl.) S157 (1996)
25. Mamyrin, B. A. & Tolstikhin, I. N. *Helium Isotopes in Nature* (Elsevier, Amsterdam, 1984).
26. CLIMAP. The surface of the ice-age Earth. *Science* **191**, 1131–1137 (1976).

27. Rostek, F. *et al.* Reconstructing sea surface temperature and salinity using δ^{18}O and alkenone records. *Nature* **364,** 319–321 (1993).

28. Rind, D. & Peteet, D. Terrestrial conditions at the last glacial maximum and CLIMAP sea-surface temperature estimates: Are they consistent? *Quat. Res.* **24,** 1–22 (1985).

29. Thompson, L. G. *et al.* Late glacial stage and holocene tropical ice core records from Huascarán, Peru. *Science* **269,** 46–50 (1995).

30. Benson, B. B. & Krause, D. Isotopic fractionation of helium during solution: A probe for the liquid state. *J. Solut. Chem.* **9,** 895–909 (1980).

···

The plastic deformation of iron at pressures of the Earth's inner core

H.-R. Wenk*, S. Matthies*, R. J. Hemley†, H.-K. Mao† & J. Shu†

* *Department of Geology and Geophysics, University of California, Berkeley, California 94720, USA*
† *Geophysical Laboratory and Center for High-Pressure Research, Carnegie Institution of Washington, Washington DC 20015, USA*

···

Soon after the discovery of seismic anisotropy in the Earth's inner core[1], it was suggested that crystal alignment attained during deformation might be responsible[2]. Since then, several other mechanisms have been proposed to account for the observed anisotropy[3,4], but the lack of deformation experiments performed at the extreme pressure conditions corresponding to the solid inner core has limited our ability to determine which deformation mechanism applies to this region of the Earth[5]. Here we determine directly the elastic and plastic deformation mechanism of iron at pressures of the Earth's core, from synchrotron X-ray diffraction measurements of iron, under imposed axial stress, in diamond-anvil cells. The ε-iron (hexagonally close packed) crystals display strong preferred orientation, with *c*-axes parallel to the axis of the diamond-anvil cell. Polycrystal plasticity theory predicts an alignment of *c*-axes parallel to the compression direction as a result of basal slip, if basal slip is either the primary or a secondary slip system. The experiments provide direct observations of deformation mechanisms that occur in the Earth's inner core, and introduce a method for investigating, within the laboratory, the rheology of materials at extreme pressures.

Much of the solid Earth undergoes intense ductile deformation. Experiments at moderate pressure and temperature have provided information about deformation mechanisms of the important rock-forming minerals in the crust and upper mantle, with olivine, quartz and calcite receiving most attention. It has been well established that intracrystalline deformation causes reorientations of crystals. The orientation pattern (or texture) in a polycrystal is indicative of both the deformation history and the mechanisms. On a macroscopic scale, texture causes anisotropy of physical properties such as propagation of seismic waves.

Here we present a method for performing deformation experiments with diamond-anvil cells, analysing the polycrystal texture *in situ*, and interpreting from it the deformation mechanisms at pressures up to that of the Earth's core. It is generally agreed that the solid inner core is composed of a nickel-containing iron alloy. Theoretical[6,7] as well as experimental studies[8–11] have examined the phase diagram of iron at high pressure, and it is likely that iron exists

as ε-iron[4]. Application of this technique to iron at pressures above 200 GPa reveals ductile deformation mechanisms that may be the key to a better understanding of the origin of elastic anisotropy of the inner core.

In recent experiments, the conventional megabar diamond-anvil cell configuration was modified to observe diffraction from lattice planes oriented at different angles relative to the diamond-anvil axis[12–14] (Fig. 1). The polychromatic synchrotron X-rays are incident on the sample at 84° to the diamond-anvil axis and diffraction patterns are recorded with an energy-dispersive detector in a symmetrical position ($2\theta = 12°$). During an experiment, the cell is rotated around an axis perpendicular to the diamond-anvil axis to bring different lattice planes into diffraction condition. Two experiments were performed at the superconducting wiggler beamline X17C at Brookhaven National Laboratory. Run 1 reached 54 GPa; the 10-μm thick, 20-μm diameter iron powder sample, of grain-size 0.1–0.5 μm, was compressed in a beryllium gasket between flat diamond anvils of 300-μm diameter and probed by a 20-μm X-ray beam. Run 2 reached 220 GPa; the 5-μm thick by 15-μm diameter specimen was compressed between bevelled diamond anvils (500-μm outer diameter, 90-μm inner diameter, 9.5° bevel angle) and probed by a 15-μm X-ray beam. Each pattern took 10 minutes to record for the larger sample in run 1, and 60 minutes for the smaller sample in run 2. Figure 2 reveals regular variations in peak intensities with rotation angle χ. There are also systematic differences in *d*-spacings of spectra for lattice planes oriented perpendicular and parallel to the diamond axis. Shifts in *d*-spacings can be explained in terms of elastic deformation under stress[14], whereas the variations in intensities are due to crystal alignment attained during plastic deformation. Whereas the intensity variations are obstacles for crystal structure refinements, they offer unique opportunities for interpreting mechanical characteristics.

For eight diffraction peaks (100, 002, 101, 102, 110, 200, 112 and 201) intensities were extracted for 10 sample orientations, corresponding to lattice planes oriented from parallel to perpendicular to the diamond-anvil axis in 10° intervals (angle χ). Intensities were integrated over the peak width in energy, and the background was subtracted. Because of incident beam intensity fluctuations, and differences in irradiated volume and absorption characteristics for different sample orientations, a preliminary normalization was performed by dividing each peak intensity by the summation of all peak intensities in a spectrum. From the relative intensity variations, the orientation distribution was calculated[15]. In the case of axial texture symmetry, results are most conveniently represented in inverse pole figures for the direction of the
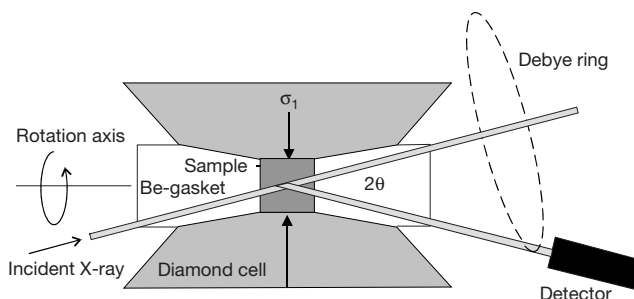

Figure 1 Experimental set-up. The deformation experiments are performed with a diamond-anvil cell positioned in a synchrotron X-ray beam. An axial stress (σ_1) that produces ductile deformation is imposed parallel to the diamond axis. The incident beam of polychromatic synchrotron X-rays and the energy-dispersive detector are arranged symmetrically with a 2θ diffraction angle of 12°. The diamond-anvil assembly is rotated around an axis perpendicular to the diamond-cell axis to record intensity variations along Debye diffraction rings.